Journal of the Mechanics and Physics of Solids 125 (2019) 550–571

Contents lists available at ScienceDirect

Journal of the Mechanics and Physics of Solids

journal homepage: www.elsevier.com/locate/jmps

Inverse design of quantum spin hall-based phononic topological insulators

S.S. Nanthakumar[c], Xiaoying Zhuang[c,d,e,*], Harold S Park[b,**], Chuong Nguyen[c], Yanyu Chen[a], Timon Rabczuk[f,g,h]

[a] Department of Mechanical Engineering, University of Louisville, Louisville, KY 40292, USA
[b] Department of Mechanical Engineering, Boston University, 110 Cummington Mall, Boston, MA 02215, USA
[c] Institute of Continuum Mechanics, Leibniz University Hannover, Appelstrasse 11A, Hannover D-30167, Germany
[d] College of Civil Engineering, Tongji University, Shanghai, China
[e] State Key Laboratory of Structural Analysis for Industrial Equipment, Dalian University of Technology, Dalian 116024, PR China
[f] Division of Computational Mechanics, Ton Duc Thang University, Ho Chi Minh City, Viet Nam
[g] Faculty of Civil Engineering, Ton Duc Thang University, Ho Chi Minh City, Viet Nam
[h] Department of Computer Engineering, College of Computer and Information Sciences, King Saud University, Riyadh 11543, Saudi Arabia

ARTICLE INFO

Article history:
Received 22 October 2018
Revised 11 January 2019
Accepted 12 January 2019
Available online 15 January 2019

ABSTRACT

We propose a computational methodology to perform inverse design of quantum spin hall effect (QSHE)-based phononic topological insulators. We first obtain two-fold degeneracy, or a Dirac cone, in the band structure using a level set-based topology optimization approach. Subsequently, four-fold degeneracy, or a double Dirac cone, is obtained by using zone folding, after which breaking of translational symmetry, which mimics the effect of strong spin-orbit coupling and which breaks the four-fold degeneracy resulting in a bandgap, is applied. We use the approach to perform inverse design of hexagonal unit cells of C_6 and C_3 symmetry. The numerical examples show that a topological domain wall with two variations of the designed metamaterials exhibit topologically protected interfacial wave propagation, and also demonstrate that larger topologically-protected bandgaps may be obtained with unit cells based on C_3 symmetry.

1. Introduction

Topological insulators (TIs) represent a new state of matter whose behavior depends only on its topology, rather than its geometry (Hazan and Kane, 2010; Moore, 2010; Qi and Zhang, 2010; Wang and Zhang, 2017). Since their theoretical prediction and subsequent experimental realization a little more than a decade ago (Bernevig et al., 2006; Kane and Mele, 2005), TIs have attracted significant interest due to their unique and exciting physical properties, namely being an insulator in the bulk while simultaneously enabling wave propagation along its boundary (Moore, 2010) or along well-defined interfaces. Because these surface states on the boundaries and interfaces of TIs are topologically protected, they are robust in the presence of defects, and have generated significant interest in controlling and guiding the propagation of acoustic, electronic,

* Corresponding author at: Institute of Continuum Mechanics, Leibniz University Hannover, Appelstrasse 11A, Hannover D-30167, Germany.
** Corresponding author.
E-mail addresses: nanthakumar@ikm.uni-hannover.de (S.S. Nanthakumar), zhuang@ikm.uni-hannover.de (X. Zhuang), parkhs@bu.edu (H.S. Park), timon.rabczuk@uni-weimar.de (T. Rabczuk).

https://doi.org/10.1016/j.jmps.2019.01.009
0022-5096/

and phononic waves that are immune not only to backscattering, but also to structural defects like cavities, disorder and sharp bends (He et al., 2016; Qi and Zhang, 2010).

While TIs originally attracted attention from the physics community, with interest in controlling the transport of electrons (Hazan and Kane, 2010), there has been significant recent interest in developing classical analogs of TIs, and several works have made connections between the quantum mechanical and classical pictures of transport (He et al., 2016; Huber, 2016; Mousavi et al., 2015; Süsstrunk and Huber, 2016). In doing so, various proposals for phononic TIs have emerged, based on either the quantum hall effect (QHE) (Chen and Wu, 2016; Kariyado and Hatsugai, 2015; Khanikaev et al., 2015; Nash et al., 2015; Nassar et al., 2017; Prodan and Prodan, 2009; Swinteck et al., 2015; Wang et al., 2015; Yang et al., 2015), the quantum spin hall effect (QSHE) (Cummer et al., 2016; He et al., 2016; Hussein et al., 2014; Mousavi et al., 2015; Pal and Ruzzene, 2017; Pal et al., 2016; 2018; Prodan et al., 2017; Süsstrunk and Huber, 2015; 2016; Xiao et al., 2015; Yu et al., 2018), and also the quantum valley hall effect (QVHE) (Chen et al., 2018a; Jiang et al., 2018; Liu and Semperlotti, 2018; Pal and Ruzzene, 2017; Ren et al., 2016; Vila et al., 2017; Wu et al., 2018; Zhu et al., 2018).

Thus, while significant success has been achieved with regards to deriving classical analogs of TIs based on the QHE, QSHE, and QVHE, the vast majority of those investigations, with few exceptions (Chen et al., 2018b; Li et al., 2018; Mousavi et al., 2015; Yu et al., 2018) have been on discrete mechanical lattices (Huber, 2016; Kane and Lubensky, 2014; Lubensky et al., 2015; Pal and Ruzzene, 2017; Pal et al., 2016; Paulose et al., 2015; Rocklin et al., 2016; 2017; Süsstrunk and Huber, 2015; Wang et al., 2015; Wu et al., 2018), rather than a continuous solid (Mousavi et al., 2015; Yu et al., 2018). This also holds true for recent experimental studies, which have also used discrete elements to achieve topologically protected wave propagation (Dong et al., 2017; He et al., 2016; Wu et al., 2018). While lattice structures such as Maxwell lattices (Chen et al., 2018a; Lubensky et al., 2015) are theoretically elegant and lend themselves to significant physical insight, many applications of interest will require continuous solids, rather than discrete lattices. Furthermore, while there has been previous work on using topology optimization and design principles for phononic crystals and acoustic metamaterials to create bandgaps and maximize the bandgap width (Yi and Youn, 2016), it is currently unknown how to design solid QSHE-based phononic TIs.

In this work, we propose a computational framework to perform inverse design of QSHE-based phononic topological insulators. We first use topology optimization to generate a Dirac cone in the bandstructure of hexagonal unit cells with C_6 or C_3 symmetry. We then use zone folding (Brendel et al., 2018; Deng and Jing, 2017; Xia et al., 2017a) to create a double Dirac cone. Finally, by breaking translational symmetry in the unit cell to mimic strong spin-orbit coupling, we are able to open a topologically non-trivial bandgap. The numerical examples demonstrate the existence of topologically-protected interface phonons in metamaterials based on the inverse designed unit cells.

2. Background on topological insulators: Parallels between quantum and classical mechanics

As discussed in the introduction, research on TIs originated in the physics community, with interest in controllably guiding the transport of electrons (Hazan and Kane, 2010). Since then, interest has spread to other communities, for example in phononics. Various works have investigated connections between quantum mechanical and classical pictures of transport, i.e. (He et al., 2016; Huber, 2016; Mousavi et al., 2015; Süsstrunk and Huber, 2016). While the interested reader is referred to those works for a more complete discussion, our objective in this section is to not only summarize the physical picture for two important quantum phenomena that form the basis for TI investigations, the quantum hall effect (QHE) and quantum spin hall effect (QSHE), but also to elucidate the connections between those and the analogous mechanical phenomena needed to generate topologically non-trivial phononic structures.

2.1. Quantum hall effect

The quantum hall effect (QHE) was discovered in 1980 (Haldane, 1988; v Klitzing et al., 1980). It was groundbreaking because it provided the first example of a condensed matter system in which a quantum state existed without spontaneously broken symmetry. The QHE occurs through the application of a magnetic field to a two-dimensionally (2D) confined electron gas within a semiconductor, which generates a voltage (the so-called Hall voltage) in the transverse direction. The magnetic field causes electrons within the bulk to occupy discrete energy levels, called Landau levels, that are completely occupied. However, electrons near the boundaries of the gas are constrained to move along the boundary in quantized (chiral) orbits, which means they must contain an integer number of de Broglie wavelengths, and so the integers that results from the QHE are examples of topological quantum numbers, called Chern numbers (Berry, 1984; Thouless et al., 1982). Importantly, because the electrons are constrained to move along the edges in only one direction, as illustrated in Fig. (1), back scattering is prevented. This lack of backscatter is the impetus for investigating topologically-protected, or dissipation-less, transport of energy in various physical systems.

However, because an external magnetic field is required, time-reversal symmetry is broken in QHE systems. While time-reversal symmetry can easily be broken through application of a static magnetic field in electronic and photonic systems, typical structural materials are passive and thus conserve time-reversal symmetry, which precludes the formation of the phononic analog of chiral edge states that are seen in QH-based electronic materials. Therefore, recently proposed QHE-based phononic TIs rely upon active components such as gyroscopes (Nash et al., 2015; Wang et al., 2015) that require energy input for operation and thus enable breaking of time reversal symmetry, which is a potential disadvantage for practical applications.

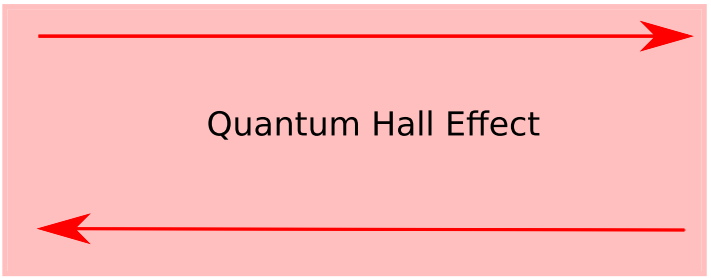

Fig. 1. Illustration of electron transport along the edges of a quantum hall semiconductor in a 1D system.

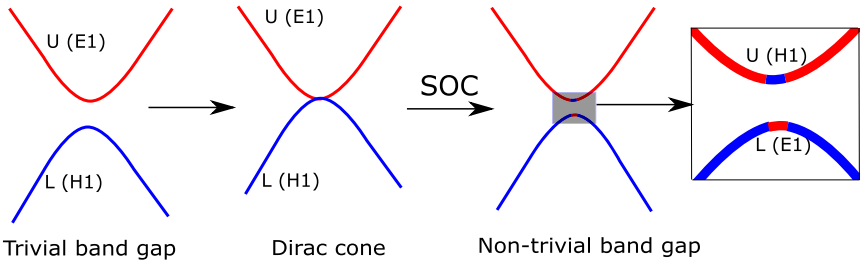

Fig. 2. Illustration of SOC and band inversion in a quantum mechanical system. The energy band "L" corresponds to a valence subband H1, and band "U" corresponds to a conduction subband E1. The SOC causes band inversion in the vicinity of the overlap or degeneracy such that "L" and "U" flip to conduction (E1) and valence (H1) subbands respectively.

2.2. Quantum spin hall effect

More recently, a new class of topological states has been both theoretically predicted (Bernevig et al., 2006; Haldane, 1988; Kane and Mele, 2005), and also experimentally observed (Konig et al., 2015). These states are known as quantum spin hall (QSH) states. It was the discovery of QSH states 10 years ago that ignited the excitement in electronic TIs within the scientific community.

Work on QSH-based TIs originated from the question of whether a QH-like effect could be observed without needing an external magnetic field. Indeed, early theoretical predictions (Bernevig et al., 2006; Haldane, 1988; Kane and Mele, 2005) hypothesized that the QHE could occur without an external magnetic field. Subsequent experiments (Konig et al., 2015) demonstrated QSHE-based topological insulation in a HgTe/CdTe quantum well. In contrast to the QHE, the effect of the magnetic field in the QSHE emerges through an effect that is universal to all materials, spin-orbit coupling (SOC) (Haldane, 1988; Manchon et al., 2015; Murakami et al., 2004). SOC refers to the interaction of a particle (i.e. an electron) with its motion, and as such, SOC can be understood as a momentum-dependent magnetic field that couples to the spin of the electrons. SOC links the orbital motion to the spin direction and acts like an external field that points in a spin-dependent direction.

Thus, while SOC occurs in all materials, only a few materials are TIs. Specifically, SOC appears to occur most easily in compounds containing heavy elements, such as Hg and Te due to the mechanism of band inversion (Bernevig et al., 2006). If spin-orbit interactions are particularly strong, the ordering of the conduction and valence bands in a semiconductor can be inverted, where the p-orbital dominated valence bands are pushed above the s-orbital dominated conduction bands (Weng et al., 2014). Furthermore, when SOC effects are strong, the two bands will open a gap, resulting in the system developing insulating properties. The process of band inversion due to strong SOC is illustrated in Fig. 2.

As a result, the QSHE leads to a topological state in which time reversal symmetry is preserved as no magnetic field is required to induce a bandgap. The edge states in QHE are chiral while QSHE insulators are helical which means at a particular edge, there are two pathways for electrons, one for the spin up state and one for the spin down state, as illustrated in Fig. 3. While electrons can travel backwards and forwards along the same edge, backscattering is still suppressed because an electron would need to flip its spin to backscatter.

In mechanical systems, the effect of strong SOC, and thus band inversion, can be seen through an inversion in the eigenmodes. Let us consider two frequency bands "L" and "U" which are below and above the band gap, respectively. As shown in Fig. 4(a), the bandstructure of topology A has a dipole eigenmode corresponding to "L" and a quadrupole eigenmode corresponding to "U". Fig. 4(b) shows the bandstructure of topology B, which has a quadrupole eigenmode corresponding to "L" and a dipole eigenmode corresponding to "U". The bandstructure of topology B is inverted as compared to topology A. In that case, a heterostructure made of topology A/B mimics, in a mechanical system, the HgTe/CdTe quantum well structure that was the first demonstration of an electronic QSHE system by Bernevig and co-workers (Bernevig et al., 2006).

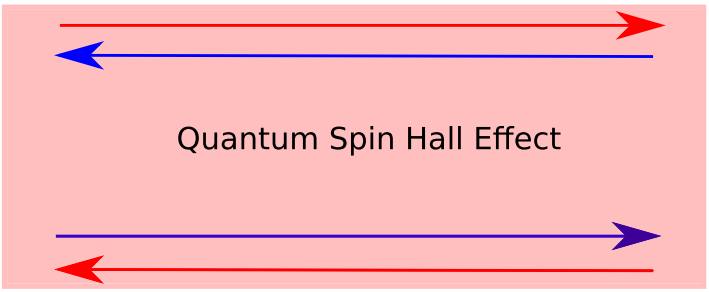

Fig. 3. Illustration of electron transport along the edge of a QSH semiconductor in a 1D system. There are four degrees of freedom: a right mover with spin up (red arrow) and a left mover with spin down (blue arrow) at the top edge, and at the bottom edge, a right mover with spin down (blue arrow) and a left mover with spin up (red arrow). (For interpretation of the references to colour in this figure legend, the reader is referred to the web version of this article.)

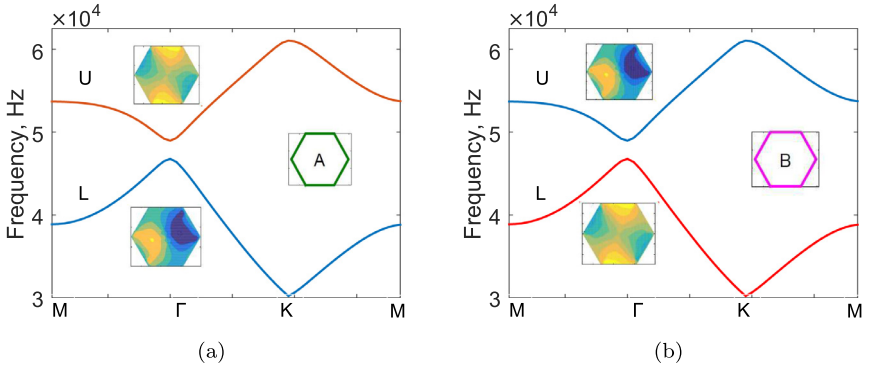

Fig. 4. Illustration of band inversion in a mechanical structure mimicking strong SOC in electronic systems. (a) Bandstructure of Topology A, (b) Bandstructure of Topology B with inverted eigenmodes between bands "L" and "U" compared to bandstructure of Topology A.

While band inversion in complex quantum well heterostructures is one approach by which the QSHE can be realized (Bernevig et al., 2006), a more influential approach with regards to establishing classical analogs of quantum phenomena that has been widely utilized in recent years is the description of a possible QSHE in graphene proposed by Kane and Mele (2005). For graphene, the Hamiltonian gives a band structure without any energy band gap. Kane and Mele (2005) proved that the SOC term cannot be ignored and has to be included in the Hamiltonian. The Hamiltonian involves two independent integer quantum Hall effects for spin up and spin down, which are referred to as pseudospins in the classical literature. Furthermore, they showed that if the SOC is sufficiently strong, it leads to the formation of a band gap and emergence of the QSHE in graphene.

While graphene does not have sufficiently strong SOC to exhibit the QSHE, researchers have exploited the hexagonal lattice structure of graphene as a starting point for developing classical analogs of the QSHE in both continuous (Li et al., 2018; Mousavi et al., 2015; Yu et al., 2018) and discrete systems (Chen et al., 2018b). Specifically, researchers start from a hexagonal structure, which does not have a topologically non-trivial bandgap (as graphene does not). While graphene does not have a bandgap, it does exhibit a Dirac cone, in which the conductance and valence bands are degenerate at a point in the energy-momentum space (Neto et al., 2009) as illustrated in Fig. 2.

To open a topologically non-trivial bandgap, the effect of SOC must be mimicked in a phononic system, which thus entails obtaining a Dirac cone, followed by introducing strong SOC to induce band inversion. To-date, there have been two successful approaches within the context of continuous, mechanical systems. In both works (Mousavi et al., 2015; Yu et al., 2018), the initial Dirac cone was obtained through starting with a hexagonal lattice structure. Subsequently, Mousavi et al. (2015) were able to successfully mimic strong SOC by breaking symmetry in the z-direction of the hexagonal structure, which induced band inversion between the "U" and "L" modes similar to the depiction in Fig. 4(a) and 4(b). Alternatively, Yu and co-workers (Yu et al., 2018) achieved strong SOC by modifying the size and spacing between hexagonal unit cells, which also alters the eigenstate between "U" and "L" modes, which is similar to the approach taken in the present work. A summary of the above discussion and the analogies between quantum and classical systems is provided in Table 1.

3. Elastic wave equation and finite element formulation

We consider in this work wave propagation in a two-dimensional solid where the dimensions of the solid in the z (out of plane) direction are much larger than the x and y (in-plane) directions. Therefore, the out of plane z mode is completely

Table 1
Quantum Spin Hall effect and its elastic analogue.

Attributes	Quantum mechanics	Classical mechanics
Governing equation	Schrödinger equation	Newton's equation of motion
Band structure	Energy in eV vs wave vector	Frequency in Hz vs wave vector
Topological band gap	due to spin orbit coupling	due to symmetry breaking
Band inversion	In case of HgTe/CdTe QWs, between valence and conduction bands of opposite parity	In case of C_{6v} symmetry phononic unit cell, Topology A/B with flip in eigenmodes

decoupled from the in-plane modes (Li et al., 2017), and thus we consider only out of plane (z-direction) displacements in this work. The governing equation for the propagation of elastic waves in a linear elastic isotropic medium is given by, assuming no body forces,

$$\nabla \cdot \boldsymbol{\sigma}(\boldsymbol{u}) = \rho \ddot{\boldsymbol{u}}, \tag{1}$$

where ρ is the density, $\boldsymbol{u}$ is the displacement vector, $\boldsymbol{\sigma}$ is the stress tensor given by $\boldsymbol{\sigma} = \boldsymbol{C} : \boldsymbol{\epsilon}$, $\boldsymbol{\epsilon}$ is the strain tensor and $\boldsymbol{C}$ is the elastic stiffness tensor of the medium.

We will consider a periodic array of hexagonal unit cells as in a metamaterial, for which the displacements, i.e. the solution of the governing Eq. (1) has to satisfy Bloch's theorem. By assuming that the free vibrational motion to be simple harmonic, the displacement at any point in the unit cell is given by

$$\boldsymbol{u}(\boldsymbol{r}, \boldsymbol{k}) = \boldsymbol{u_k}(\boldsymbol{r}) e^{\boldsymbol{i}(\boldsymbol{kr})}, \tag{2}$$

where $\boldsymbol{u_k}$ is the amplitude vector with the same periodicity as the structure, $\boldsymbol{r}$ is the position vector and $\boldsymbol{k}$ is the wave vector.

We adopt standard finite element (FE) techniques to approximate the displacement $\boldsymbol{u}$ such that numerical solutions to the governing Eq. (1) can be found. Specifically, we utilize standard bilinear 4-node quadrilateral elements to discretize the domain, where the z-direction (out of plane) displacement is the only degree of freedom for each node. The discrete system of equations for the associated eigenvalue problem is given by

$$[\boldsymbol{K}(\boldsymbol{k}) - \omega^2 \boldsymbol{M}]\boldsymbol{U} = 0, \tag{3}$$

where $\boldsymbol{K}$ and $\boldsymbol{M}$ are the stiffness and mass matrix of the unit cell, the wave vector $\boldsymbol{k}$ comprises wave vector coordinates that lie along the boundary of the irreducible Brillouin zone, and where the eigenvectors $\boldsymbol{U}$ represent the modes of deformation of the unit cell for each frequency ω. The band structure or dispersion diagram can be obtained by plotting the natural frequency ω as a function of wave vector $\boldsymbol{k}$. The boundaries of the irreducible Brilluoin zone of a hexagonal unit cell with lattice constant a are

$$\begin{aligned}
\Gamma M &= \left(k\,,\ \frac{k}{\sqrt{3}} \right),\ 0 < k < \frac{\pi}{a} \\
MK &= \left(\frac{\pi}{a} - k_1\,,\ \frac{\pi}{a\sqrt{3}} - k_2 \right),\ 0 < k_1 < \frac{\pi}{3a};\ 0 < k_2 < \frac{\pi}{a\sqrt{3}} \\
K\Gamma &= \left(\frac{2\pi}{3a} + k_1\,,\ \frac{2\pi}{a\sqrt{3}} + k_2 \right),\ 0 > k_1 > -\frac{2\pi}{3a};\ 0 > k_2 > -\frac{2\pi}{a\sqrt{3}}
\end{aligned} \tag{4}$$

4. Requirements for quantum spin hall-based phononic topological insulators

Before describing the inverse computational methodology, it is necessary to first define the physical constraints that a QSHE-based phononic TI should satisfy. Such requirements were first laid out in the seminal work of Mousavi et al. (2015), which we detail now. The first step is to generate a Dirac cone in the bandstructure. As has been discussed in the literature (Lu et al., 2014; van Miert and Smith, 2016), there are certain symmetries that allow Dirac cones, in particular graphene-like unit cells with triangular symmetry, which leads to a Dirac cone for phonons at the K and K' points (Mousavi et al., 2015). Furthermore, the C6 and C3 symmetries are two symmetries for which Dirac cones exist (Lu et al., 2014), and so we adopt unit cells with those configurations in this work. As will be described in more detail below, we will use topology optimization to get the initial Dirac cone in the hexagonal unit cells, for both C6 and C3 symmetries.

Once the initial Dirac cone is obtained, a second, degenerate Dirac cone is required. Two degenerate Dirac cones are required to mimic the two degenerate spin states in graphene. In the present work, once the first Dirac cone is obtained via topology optimization, we utilize zone folding (Xia et al., 2017b; Zhang et al., 2017) to obtain the doubly degenerate Dirac cones. Once the doubly degenerate Dirac cones are obtained, we break translational symmetry of the unit cell to achieve both topologically trivial and non-trivial unit cells. By bulk-boundary correspondance (Hazan and Kane, 2010), an interface that is created between topologically trivial and non-trivial unit cells will support the propagation of topologically protected phonons.

5. Topology optimization for single dirac cone

To obtain a Dirac cone, in which degenerate modes are constructed by matching the frequency of different modes in a hexagonal unit cell, we perform topology optimization. Because all modes in our 2D problem are out of plane (flexural), practically this entails matching the frequency of two consecutive modes at the K point in a hexagonal unit cell. We note that due to the kinematic assumptions used, complex, multi-scale microstructures such as those developed by Mousavi et al. (2015) to obtain degeneracy between symmetric and anti-symmetric modes are not needed in this work. One area for future work is to extend the proposed methodology for this more general problem.

The topology optimization problem is solved by using a level set based optimization scheme (Allaire et al., 2004). The spin degeneracy requirement can be posed as an optimization problem with the following multiple objective functions,

$$\begin{aligned} & J1 = -\omega_{1k} \\ & J2 = \omega_{2k} \\ & J3 = |\omega_{1k} - \omega_{2k}| \\ \min \quad & J = J1 + J2 + J3 \end{aligned} \tag{5}$$

The first objective function, J_1, ensures that the frequency of the first mode ω_{1k} is largest at the high-symmetry K point. The second objective function, J_2, ensures that the frequency of the second mode ω_{2k} is a minimum at the K point. The final objective function, J_3, ensures that the first and second modes are degenerate at the K point.

In this work we minimize the objective functions using the parametric level set optimization method (Wang and Wang, 2006), such that the topology is represented by an implicit level set function Φ. The zero isoline of the level set function Φ represents the internal boundaries of the unit cell. When the level set function Φ moves in the normal direction with a velocity, V_n, it satisfies the Hamilton–Jacobi equation,

$$\frac{\partial \Phi(x)}{\partial t} + V_n |\nabla \Phi| = 0. \tag{6}$$

The explicit parametrization of the level set method using compactly supported radial basis function (CSRBF) is performed to convert the PDE in (6) into an ordinary differential equation. The level set function in terms of the CSRBF interpolant f and expansion coefficients α is

$$\Phi(\boldsymbol{x}, t) = \boldsymbol{f}(\boldsymbol{x})^T \boldsymbol{\alpha}(t) = \sum_{i=1}^{n} f_i(\boldsymbol{x})\, \alpha_i, \tag{7}$$

where n is the number of knots. The advantage of explicit parametrization of the level set function using CSRBF is that the unknowns in each iteration are not the nodal level set values but the expansion coefficients of the interpolation. Substituting Eq. (7) into the Hamilton–Jacobi Eq. (6) reduces the HJ equation into an ODE as shown below,

$$\boldsymbol{f}^T \frac{d\boldsymbol{\alpha}}{dt} + V_n |(\boldsymbol{\nabla f})^T \boldsymbol{\alpha}| = 0. \tag{8}$$

The above equation is solved in each iteration to get the updated level set function. The CSRBF with C^2 continuity proposed by Wendland (1995) is utilized,

$$f(r) = \max\{0, (1-r)\}^4 (4r+1). \tag{9}$$

The design variables in this optimization scheme are the expansion coefficients, $\boldsymbol{\alpha}$. The gradient of the eigenfrequency with respect to design variables is given by,

$$\frac{\partial \omega_n}{\partial \alpha} = \frac{1}{\omega_n}\, u(k)^T \left(\frac{\partial K}{\partial \alpha} - \omega_n^2 \frac{\partial M}{\partial \alpha} \right) u(k) \tag{10}$$

We illustrate in Fig. 5a–5(e) the necessity of having all three objective functions J_1, J_2 and J_3 being simultaneously minimized. Fig. 5(a) shows the dispersion curves for the first and second modes for a hexagonal unit cell which minimizes only objective function J_1. As can be seen, in this case the modes are not degenerate at the K point, and the second mode is not a minimum at the K point. If both J_1 and J_2 are minimized, then the bandstructure is as shown in Fig. 5(b), where the first mode is maximized and the second mode is minimized at the K point, but they are still not degenerate. If all the objective functions (J_1, J_2 and J_3) are minimized, then the obtained bandstructure will have a Dirac point as shown in Fig. 5(c). It is evident that the degeneracy is imposed by minimizing J_3.

In case of higher symmetries like C_{6v} and C_6, the bandstructure can have several Dirac degeneracies, but they may not be suitable for obtaining a complete topological band gap. For example, in the band structure shown in Fig. 5(d), only J_3 is minimized which results in a Dirac cone at the K point. However, when a bandgap is opened at the Dirac point, the bandgap is a partial, and not complete bandgap as shown in (Fig. 5(e)). Thus, though hexagonal unit cells with C_{6v} and C_6 symmetries may have many Dirac degeneracies at the K-point in their bandstructure, they can be utilized as a phononic TI only if all the objective functions J_1, J_2 and J_3 are simultaneously minimized.

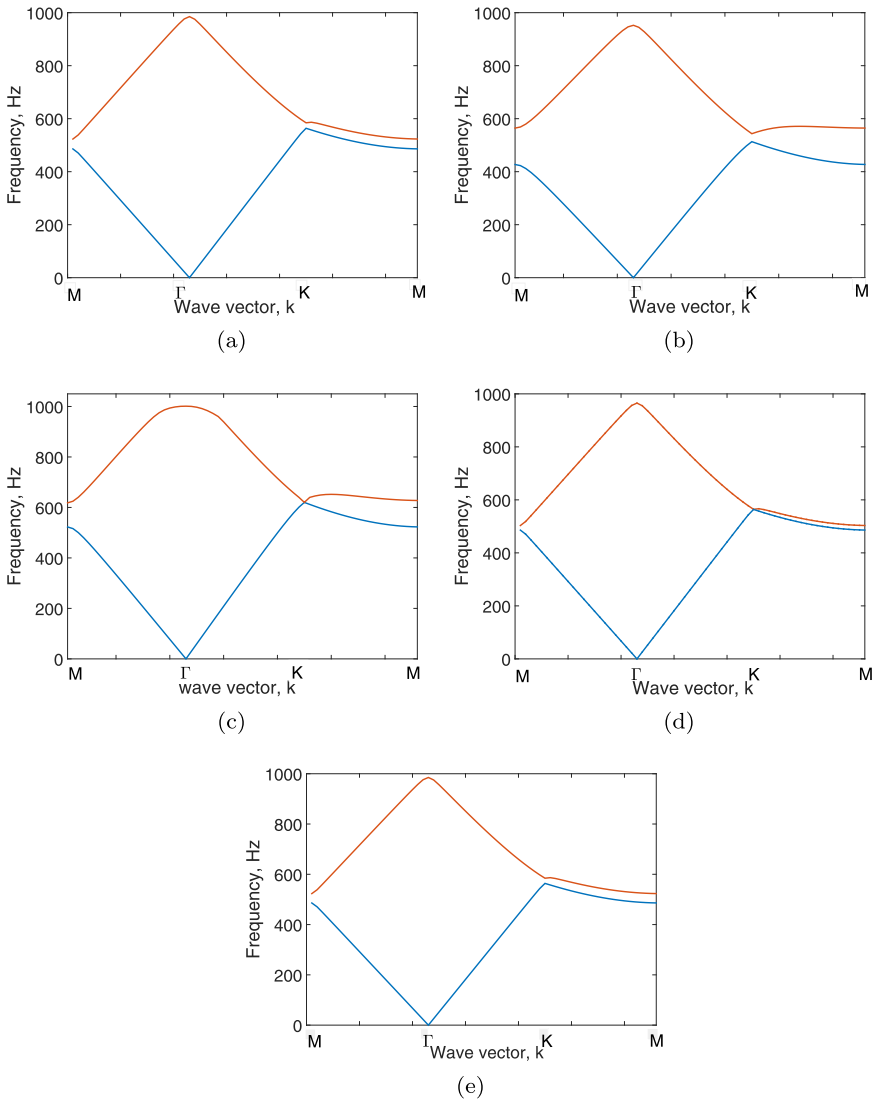

Fig. 5. Bandstructure of the unit cell that minimizes (a) J_1, (b) J_1 and J_2, (c) J_1, J_2, J_3 and (d) J_3, (e) Bandstructure with partial band gap.

6. Four-fold degeneracy and band gap opening

6.1. Zone folding mechanism

Once the single Dirac cone is obtained via topology optimization, as illustrated in Fig. 5(c), the question to consider is how to obtain a doubly degenerate Dirac cone. We accomplish this in the present work using a zone folding approach (Xia et al., 2017b; Zhang et al., 2017), where the concept is illustrated in Fig. 6. Similar to the direct lattice, the reciprocal lattice is also periodic. All the wave vector points in the first Brillouin zone are unique, while the wave vector points in the higher Brillouin zones can be projected back to the first zone. The idea behind zone folding is to utilize a larger hexagonal unit cell colored in red in Fig. 6(a), which comprises several primitive hexagonal unit cells in blue. The lattice constant of the basic and large unit cell are a_0 and a respectively, such that $a = a_0\sqrt{3}$. The first Brillouin zone of the original hexagonal unit cell is shown in blue in Fig. 6(b), the first Brillouin zone of the large unit cell is shown in red. By surfing through the wave vector points along the path $M_1 - \Gamma_1 - K_1 - M_1$, the bandstructure of the original hexagonal unit cell in Fig. 6(a) can be obtained. The bandstructure of the larger hexagonal unit cell in Fig. 6(b) can be obtained by surfing through $M_2 - \Gamma_2 - K_2 - M_2$. The bandstructure of larger hexagonal unit cell in Fig. 6(a) can also be obtained by folding or mapping the region $M_1 - K_1 - K_2 - M_1$ to $M_2 - K_1 - K_2 - M_2$ and then onto $M_2 - \Gamma_1 - K_2 - M_2$. This means that $M_2 - \Gamma_2 - K_2 - M_2 = M_1 - K_1 - K_2 - M_1 + M_2 - K_1 - K_2 - M_2 + M_2 - \Gamma_1 - K_2 - M_2$ as shown in Fig. 6(c). This zone folding mechanism shows that the band curve at K_1 maps onto Γ_2 twice if the basic and large unit cell are chosen as shown in Fig. 6(a). If

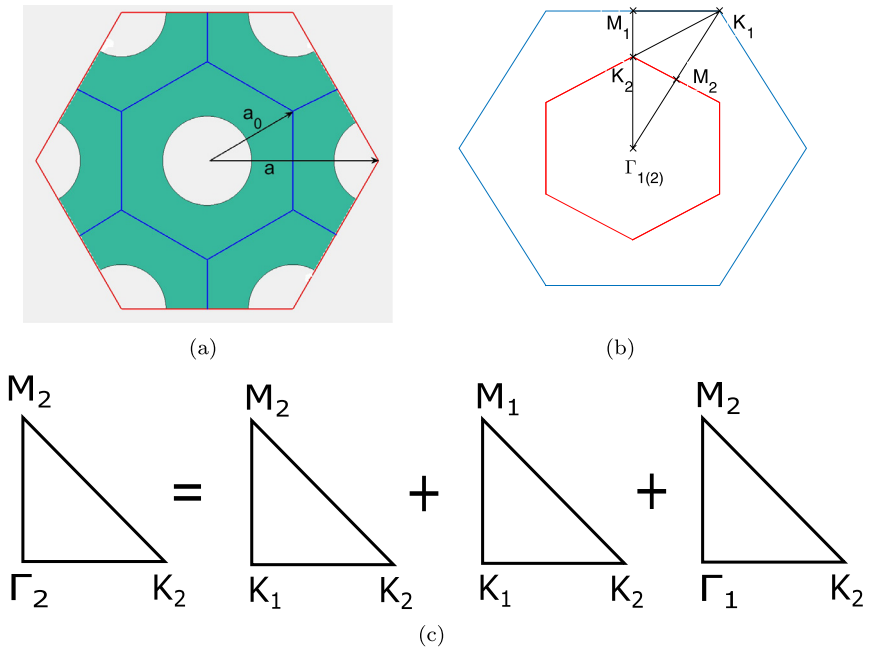

Fig. 6. (a) Basic (blue) and large (red) unit cell; (b) Brillouin zone corresponding to basic (blue) and large (red) unit cell in reciprocal space; (c) The zone folding process. (For interpretation of the references to colour in this figure legend, the reader is referred to the web version of this article.)

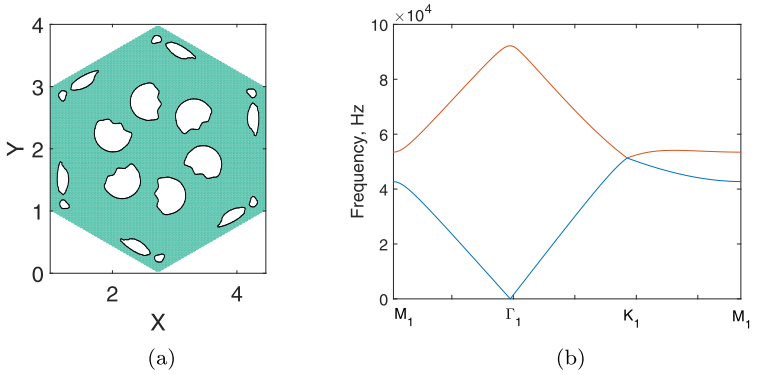

Fig. 7. (a) Topology of hexagonal basic unit cell (lattice constant, $a_0 = 2$ cm); (b) Band structure of hexagonal basic unit cell.

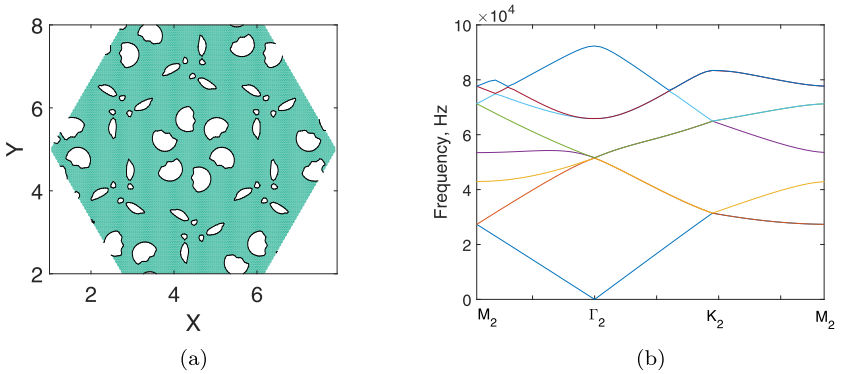

Fig. 8. (a) Topology of hexagonal large unit cell obtained from basic unit cell shown in Fig. 7 (lattice constant, $a = 2\sqrt{3}$ cm); (b) Band structure of hexagonal large unit cell.

a two-fold degeneracy exists at K_1, then enlarging the unit cell as in Fig. 6(a) leads to two, two-fold degeneracies at the Γ point, i.e. a four-fold degeneracy at Γ_2. Therefore once a topology with two-fold degeneracy is obtained by topology optimization, the zone folding mechanism helps in obtaining the four-fold (double Dirac) degeneracy, which is an important step in obtaining a topological band gap.

6.2. Breaking symmetry

Once the unit cell with a double Dirac cone is obtained, further modifications in the unit cell are performed to reduce symmetry and open a non-trivial topological band gap. In the case of a hexagonal unit cell with C_6 symmetry, this can be done by adding or removing material at the center or at the six corners of the hexagonal unit cell. This results in breaking translational symmetry while preserving C_6 symmetry, as recently shown by Deng and Jing (2017).

In the case of a hexagonal unit cell with C_3 symmetry, the band gap can be opened by rotating the unit cell topology by an angle of 30° in either direction (Xia et al., 2017a). For both C_6 and C_3 symmetries, these unit cell modifications lead to two separate unit cells A and B in which band inversion, or a flip in the degenerate eigenmodes, takes place, which is a signature of a topological phase transition between unit cells A and B. This topological phase transition ensures that if a periodic

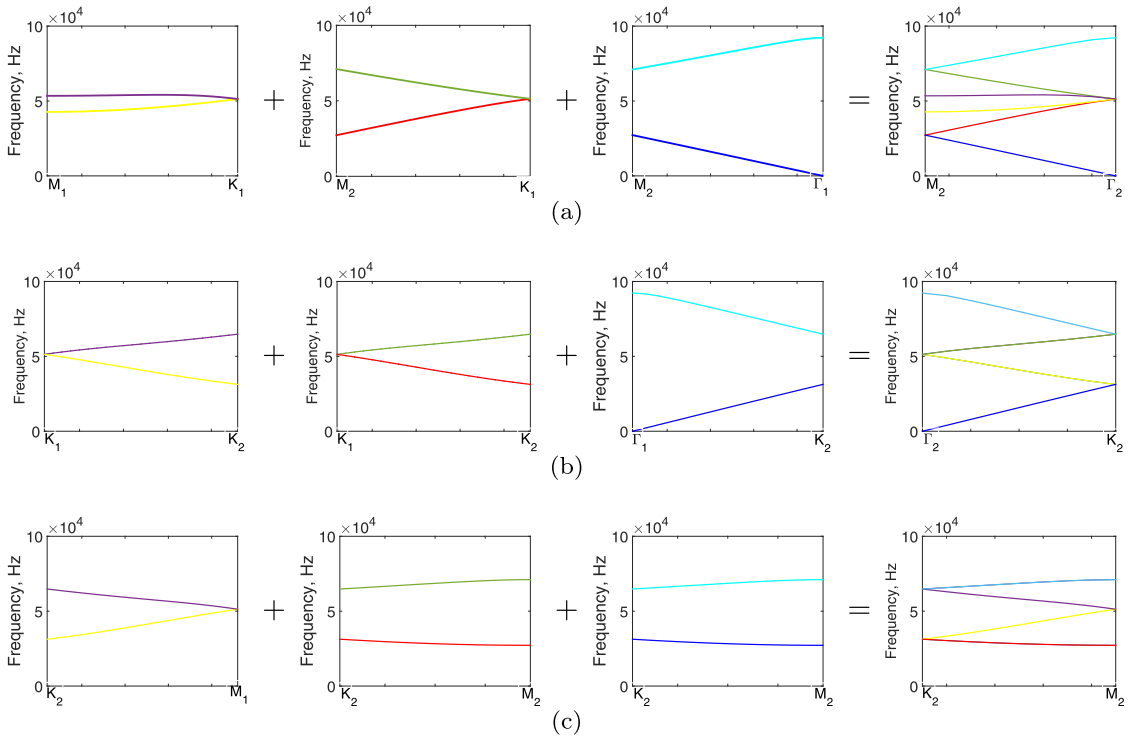

Fig. 9. The intermediate steps involved in the conversion of a two-fold degeneracy to four-fold degeneracy by adopting the zone folding mechanism.

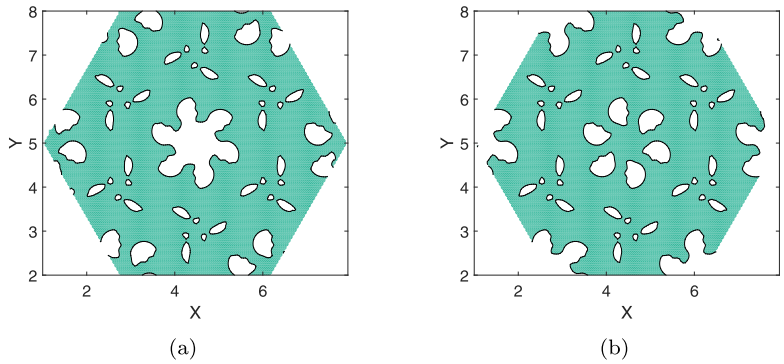

Fig. 10. Topology of enlarged unit cell (a) A, which is obtained by removing material over a circle of radius 0.5 cm from the center of the hexagonal unit cell, and (b) B, which is obtained by removing material over a circle of radius 0.5 cm from the corners of the hexagonal unit cell.

structure is constructed with an interface between unit cells A and B, the resulting interface supports topologically protected phonons via bulk-boundary correspondance (Hazan and Kane, 2010). Overall, one advantage of the present approach is that it can, given a unit cell structure, systematically find the resulting topology that leads to two-fold and subsequently four-fold degeneracy in the bandstructure. This is in contrast to previous approaches (Mousavi et al., 2015) where the four-fold degeneracy has been obtained in a more ad hoc fashion.

We note that while the approach proposed here is more systematic than previous approaches, it does not work for any arbitrary combination of modes. Specifically, the optimization problem formulated in Section 5 is suitable for the inverse design of unit cells with degeneracy between any two desired modes. However, the band opening mechanisms we used, i.e. adding and removing material from the C_6 unit cell and rotation of the C_3 unit cell, are not necessarily able to produce the band inversion between any two degenerate mode pairs, which is necessary to mimic the strong spin-orbit coupling effect. This indicates that the band inversion mechanism may be dependent on the eigenmodes, and may need to be devised specifically for different combinations of modal degeneracies.

In the following numerical examples Section 7, we demonstrate the effectiveness of the proposed approach to generate topologically-protected interfacial wave propagation.

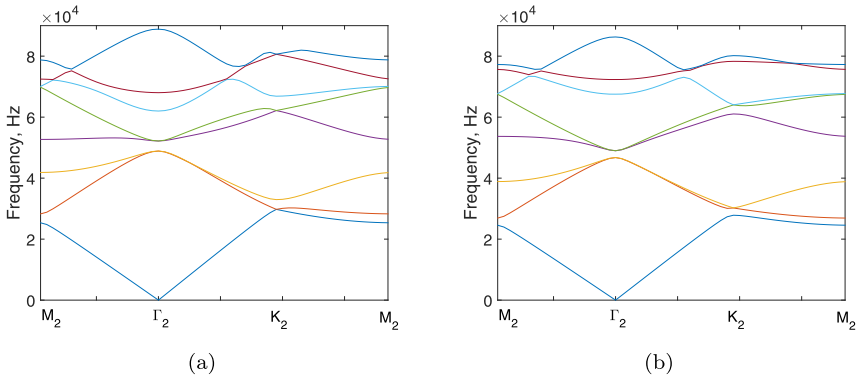

Fig. 11. (a) Band structure of modified unit cell A; (b) Bandstructure of modified unit cell B.

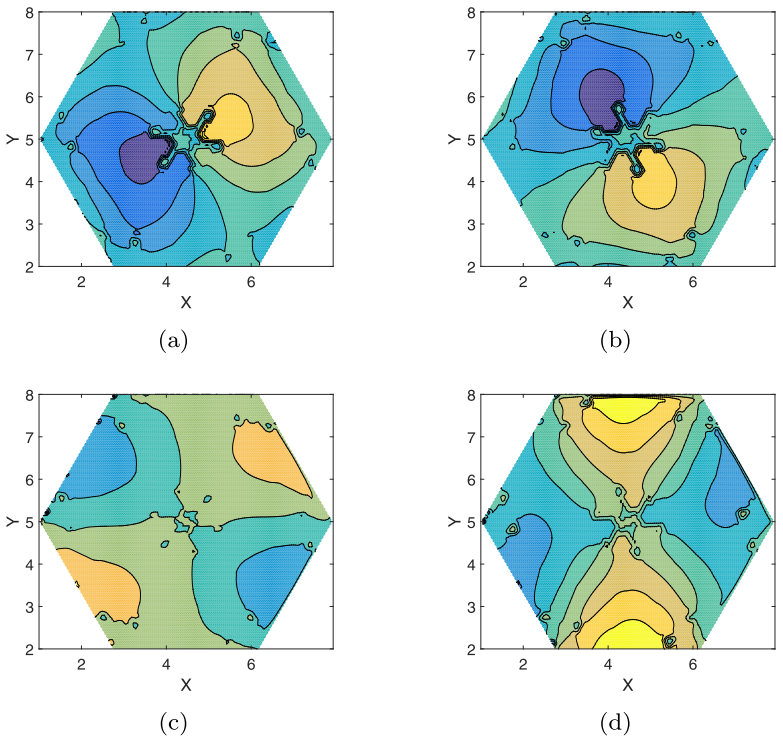

Fig. 12. Eigenmodes for modified enlarged unit cell A (a) Band 2 (b) Band 3 (c) Band 4 (d) Band 5.

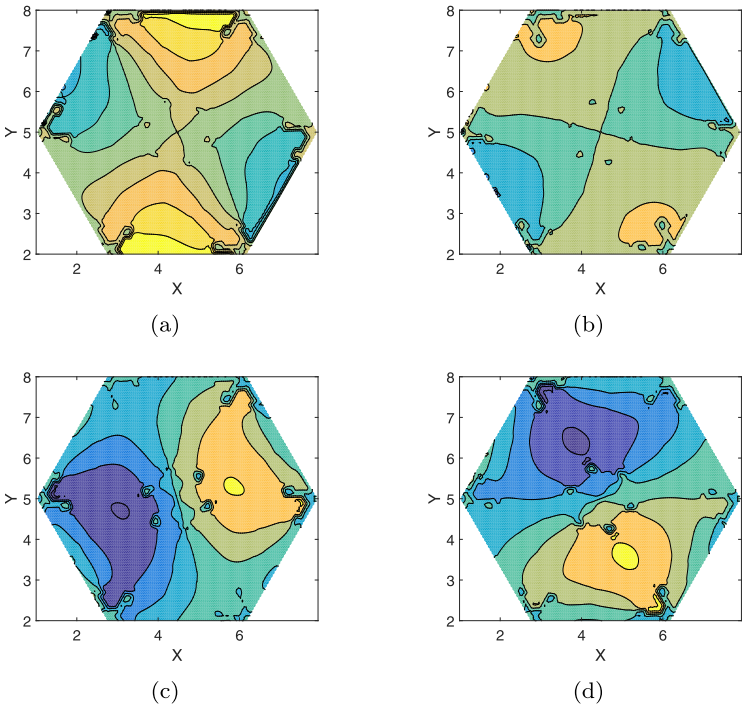

Fig. 13. Eigenmodes for enlarged modified unit cell B (a) Band 2 (b) Band 3 (c) Band 4 (d) Band 5.

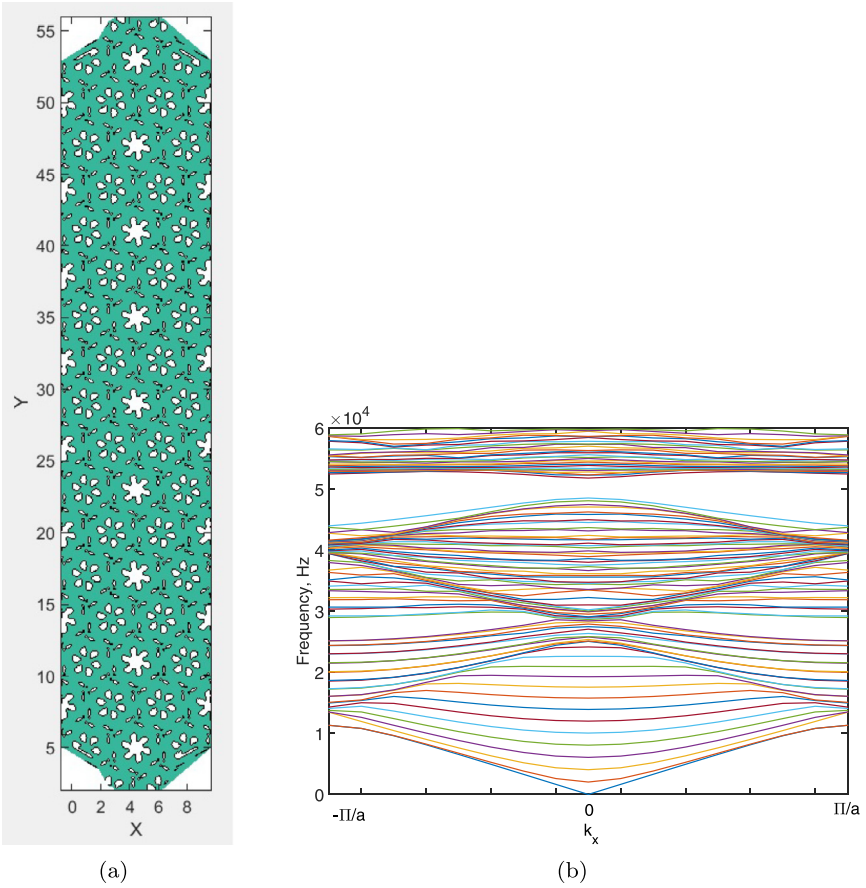

Fig. 14. (a) Supercell of unit cell A and (b) its corresponding bandstructure.

7. Numerical examples

7.1. Unit cell - C_6 symmetry

In this section, we utilize the proposed inverse design methodology to obtain double Dirac degeneracy and subsequently create a topologically non-trivial bandgap in a hexagonal unit cell with C_6 symmetry. For all cases, we assume that the unit cells are made of Aluminum, with a Young's modulus of E=69 GPa, Poisson's ratio of ν=0.35, and density ρ=2700 kg/m^3. As a first step, the hexagonal unit cell whose topology is defined by the implicit level set function is designed in which the two-fold degeneracy (a single Dirac cone) occurs at the K-point between modes 1 and 2. The hexagonal unit cell is discretized by 4-node quadrilateral finite elements. The topology is constrained to possess C_6 symmetry, and is also constrained such that the volume fraction remains larger than 50%. The unit cell topology providing the single Dirac cone is shown in Fig. 7(a), while the corresponding bandstructure is shown in Fig. 7(b).

Having obtained the two-fold degeneracy in Fig. 7(a), a four-fold degeneracy (double Dirac cone) can be created by utilizing the zone folding mechanism. The union of the bandstructure along the Brillouin zone boundaries M_1K_1, M_2K_1 and $M_2\Gamma_1$ of basic unit cell yields the band structure along $M_2\Gamma_2$ of the large unit cell. The bandstructure along the Brillouin zone boundaries K_1K_2, K_1K_2 and Γ_1K_2 of the basic unit cell combine to give the bandstructure along Γ_2K_2 of the large unit cell. The bandstructure along the Brillouin zone boundaries K_2M_1, K_2M_2 and K_2M_2 of basic unit cell combine to give the band structure along K_2M_2 of the large unit cell. Fig. 9 depicts the intermediate steps involved in the zone folding process that converts a two-fold degeneracy to a four-fold degeneracy. The enlarged unit cell obtained by enlarging the topology optimized unit cell obtained in Fig. 7(a) is shown in Fig. 8(a), while the corresponding bandstructure of the enlarged unit cell is shown in Fig. 8(b). The zone folding mechanism maps the two-fold degeneracy at the K point in the smaller unit cell in Fig. 7(a) to the Γ point for the enlarged unit cell leading to a four-fold degeneracy, thus satisfying one of the key requirements to obtaining a topologically protected phononic metamaterial based on the QSHE.

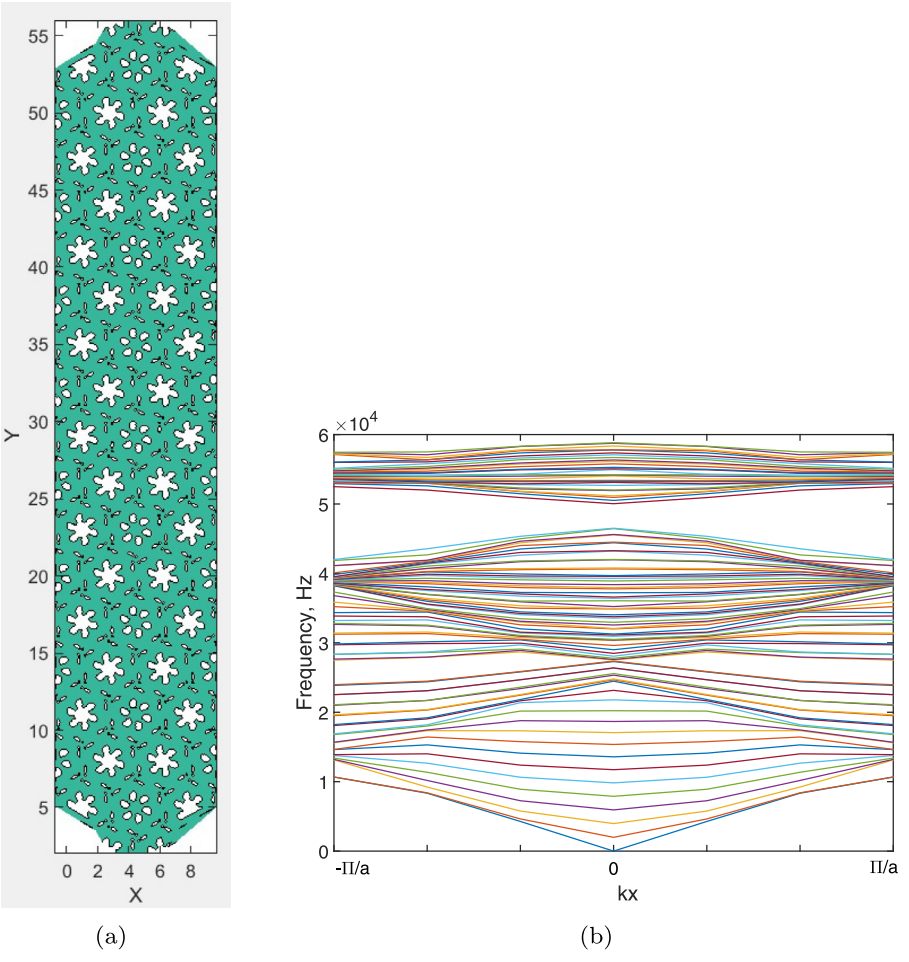

Fig. 15. (a) Supercell of unit cell B and (b) its corresponding bandstructure.

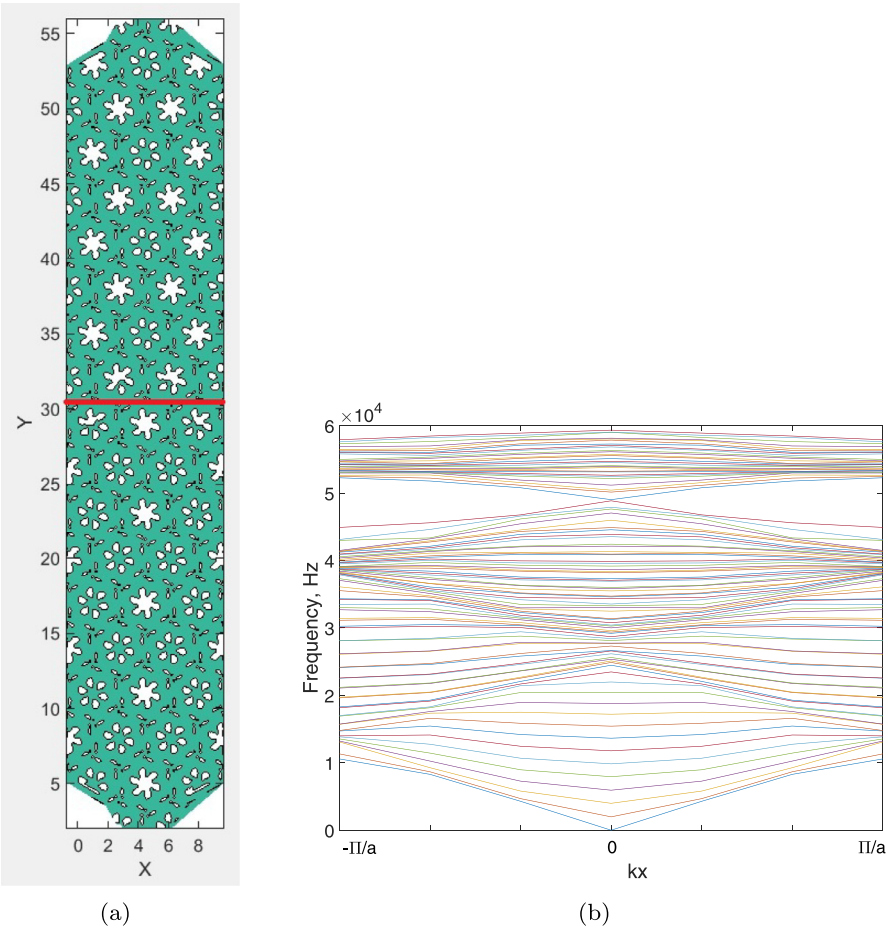

Fig. 16. (a) Supercell with interface (horizontal red line) between supercells of unit cell A and unit cell B and (b) its corresponding bandstructure. Note the presence of the edge modes that cross the bandgap. (For interpretation of the references to colour in this figure legend, the reader is referred to the web version of this article.)

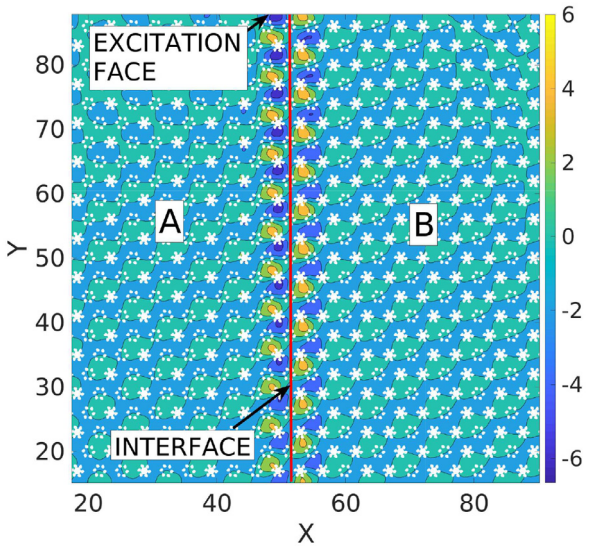

Fig. 17. Displacement contour showing topologically-protected wave propagation along a straight interface. All dimensions are in cm.

Having obtained the four-fold degeneracy, the final step is to open a topologically non-trivial bandgap. Here, the requirement is that the enlarged unit cell in Fig. 8(a), which exhibits four-fold degeneracy but no bandgap as shown in Fig. 8(b), must be modified to obtain two different unit cells which exhibit an inversion of the eigenmodes, which would mimic the strong spin-orbit coupling that is necessary in topologically non-trivial quantum mechanical systems (Mousavi et al., 2015). Doing so would remove the Dirac degeneracy at the Γ point and thus open a bandgap.

We therefore performed two different modifications of the large unit cell in Fig. 8(a), creating the modified unit cells A and B, which are shown in Fig. 10. Specifically, unit cell A is obtained by removing material in the vicinity of the center of the unit cell, where the radius of the hole introduced at the center of the unit cell is 0.5 cm. Unit cell B is obtained by removing material at the corners of the hexagonal unit cell, where again the radius over which material is removed at the corners is fixed as 0.5 cm.

The bandstructures of the modified hexagonal unit cells A and B are shown in Fig. 11. As can be seen, the modifications made to the topology offering Dirac degeneracy (Fig. 10) result in the formation of bandgaps for both modified unit cells. More importantly, we can verify that inversion of the eigenmodes is also observed in comparing the eigenmodes of the

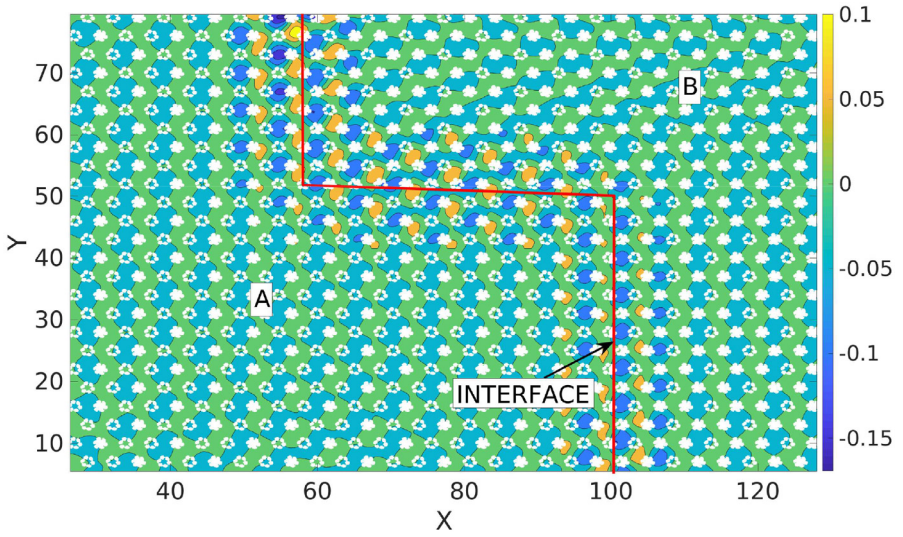

Fig. 18. Displacement contour showing propagation along a topologically-protected zig-zag interface. All dimensions are in cm.

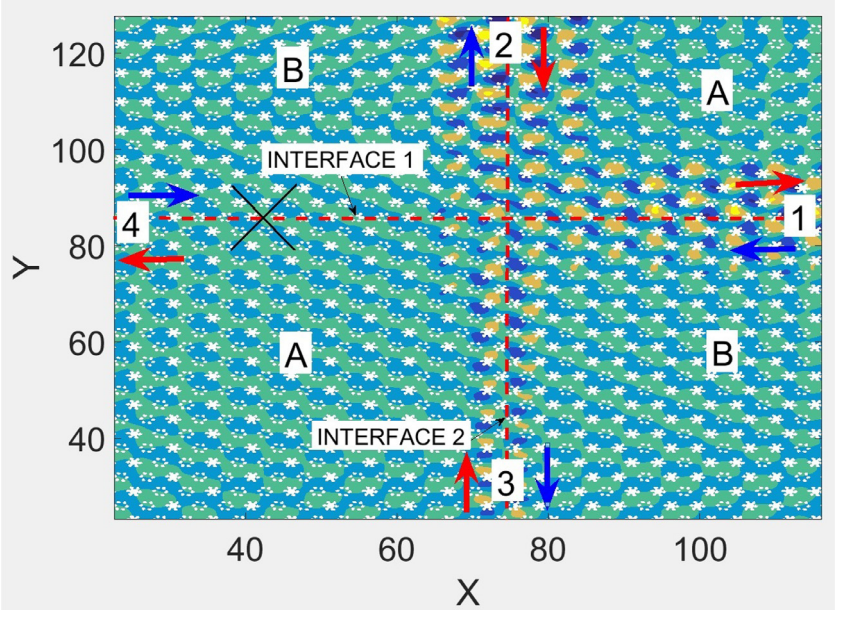

Fig. 19. Displacement contour showing propagation along two intersecting interfaces when the input excitation is from the right boundary of the structure. All dimensions are in cm (For interpretation of the references to colour in this figure, the reader is referred to the web version of this article.).

modified unit cells A and B. Specifically, the second and third eigenmodes of unit cell A in Fig. 12(a) and 12(b) are the same as the fourth and fifth eigenmodes of unit cell B shown in Fig. 13(c) and 13(d). Similarly, the fourth and fifth eigenmodes of unit cell A in Fig. 12(c) and 12(d) match the second and third eigenmodes of unit cell B shown in Fig. 13(a) and 13(b). This topological phase transition ensures that if a periodic structure is constructed with an interface between unit cells A and B, the resulting interface supports topologically protected phonons via bulk-boundary correspondence (Hazan and Kane, 2010).

To illustrate the essential role of the interface between the modified unit cells A and B in hosting the topologically protected phonons, we first created supercells made of only the modified unit cells A and B. The supercell made of unit cell A is shown in Fig. 14(a), where the supercell is periodic in the x-direction while being finite in the y-direction. The bandstructure of the supercell is shown in Fig. 14(b). A clear bandgap can be seen between 48,500 to 51,500 Hz. However, no edge modes that cross the bandgap, which are a signature of topologically non-trivial modes, are observed. The supercell made of unit cell B is shown in Fig. 15(a), with the corresponding bandstructure shown in Fig. 15(b), which shows a bandgap

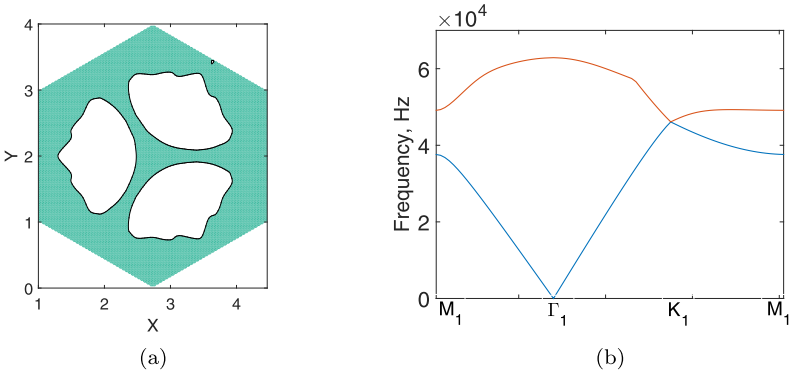

Fig. 20. (a) Topology of hexagonal unit cell with C_3 symmetry (lattice constant, $a_0 = 2$ cm) and (b) the corresponding bandstructure.

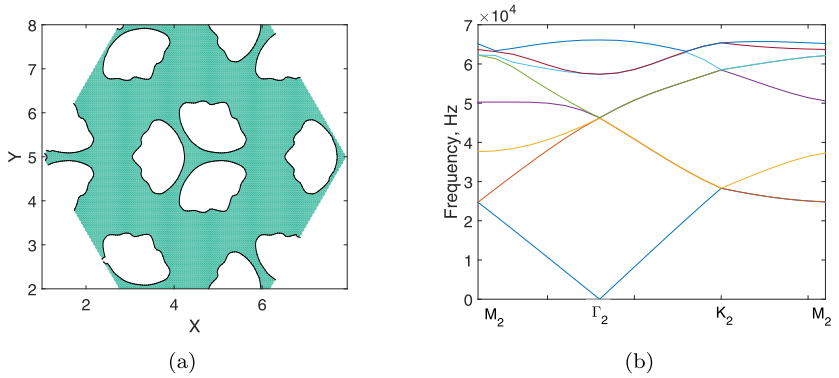

Fig. 21. (a) Topology of hexagonal large unit cell obtained from basic unit cell shown in Fig. 20 (lattice constant, $a = 2\sqrt{3}$ cm); (b) Band structure of hexagonal large unit cell.

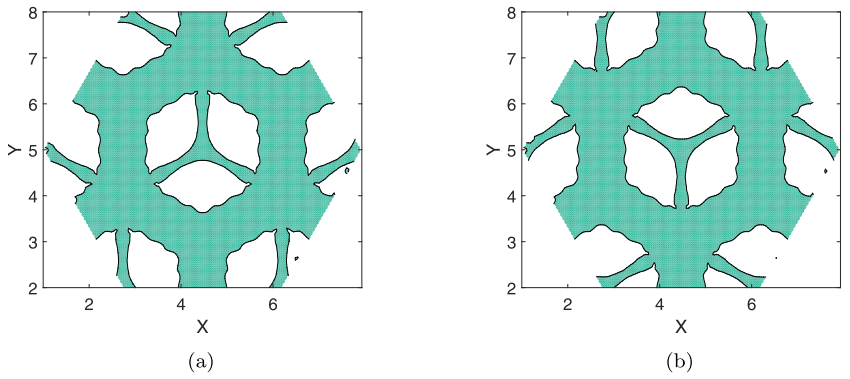

Fig. 22. Topology of hexagonal large unit cells (a) A and (b) B obtained by modifying the topology in Fig. 21.

between 46,500 to 49,500 Hz. However, as in the case with the supercell with only A unit cells, there are no edge modes that cross the bandgap for the B unit cell supercell structure.

Therefore, we created a supercell with four rows of A unit cells and five rows of B unit cells as shown in Fig. 16(a), with an interface between the A and B unit cells. The bandstructure obtained for this supercell in Fig. 16(b) not only exhibits a bandgap, but also exhibits the presence of edge modes within the bandgap. Specifically, the bandgap frequency range in Fig. 16(b) is 48,000 to 50,000 Hz, which is similar to the overlapping frequency range of the bandgaps of supercells of unit cells A and B shown in Figs. 14(b) and 15(b) respectively. These edge modes, which are often referred to as the pseudospin states, represent counter-propagating modes that carry opposite spins (Mousavi et al., 2015). As further confirmation of the existence of topologically non-trivial modes along the interface, the Berry curvatures of the four interface modes are plotted in the Appendix A and are observed to be consistent with the previous observation of band inversion.

The above results on the supercell structures were performed in the frequency domain to calculate the bandstructure. In order to validate the calculated topological bandgaps, we performed real-space FEM simulations using a periodic structure with 17 $\times$ 17 unit cells shown in Fig. 17. The periodic structure has 8 columns of A unit cells to the left of the interface and 9 columns of B unit cells to the right of the interface. For these simulations, each unit cell was discretized by 2594 four-node quadrilateral elements. The structure was fixed at Y=0, and harmonic excitation was applied at the top surface (Y=104 cm)

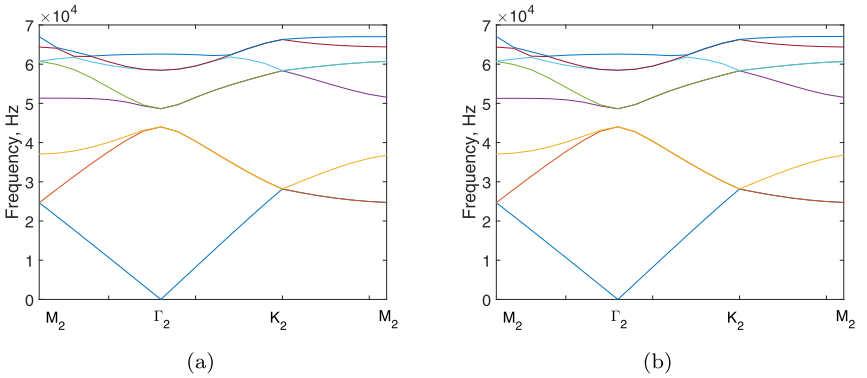

Fig. 23. Band structure of hexagonal large unit cells (a) A and (b) B shown in Fig. 22.

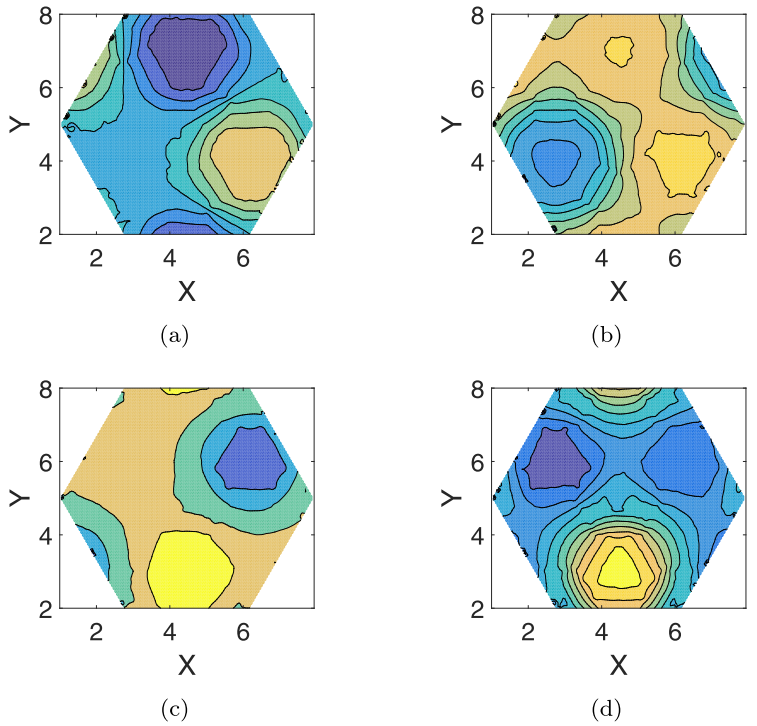

Fig. 24. Eigenmodes of unit cell A, (a) Band 2 (b) Band 3 (c) Band 4 (d) Band 5.

at a frequency of 48,900 Hz (which lies within the topologically-protected bandgap). The resulting steady state displacement field is shown in Fig. 17. The figure clearly shows the localization of displacement close to the straight interface.

We next illustrate that topologically-protected interface propagation can occur with more complex interfaces. As such, we created a zig-zag interface, in a periodic structure made of 21 $\times$ 17 unit cells, which is fixed at Y=0 and excited at Y=104 cm with a frequency of 48,900 Hz. As seen in Fig. 18, the periodic structure has A unit cells to the left of the interface and B unit cells to the right of the interface. Even with the complex zig-zag interface, the waves remain localized to the zig-zag interface, and propagate cleanly around the multiple sharp interfaces along its path.

Our final example involving the unit cells with C_6 symmetry aims to illustrate one of the unique aspects of QSHE-based interfacial wave propagation, i.e. that of spin-dependent interfacial propagation. To illustrate this feature, we constructed a periodic structure with two intersecting interfaces as shown in Fig. 19. In Fig. 19, the blue and red arrows indicate two different spin states. We first excite the structure from the right boundary. For this wave to propagate into the structure, the spin state must be the one indicated by the blue arrow. This wave thus enters the structure from the right boundary, propagates along interface 1, and then reaches the top and bottom surfaces by propagating along interface 2, which supports the blue spin state. This spin-polarized wave cannot pass through the intersection of interfaces 1 and 2 to continue along horizontal interface 1 to the left hand side due to the fact that it would have to switch spin states from blue to red in order to reach the left hand side of the structure. This demonstrates the helical nature of the interface state, i.e. that it travels only along the interfaces that align with the incoming spin state, and thus proves that the interfacial wave propagation is achieved via a QSHE analogue. This also demonstrates that uni-directional wave propagation in QSHE-based phononic TIs can be achieved through proper construction of the topological interfaces, as shown in Fig. 19.

7.2. Unit cell - C_3 symmetry

Having demonstrated the approach on a hexagonal unit cell with C_6 symmetry, we now demonstrate the inverse design methodology on a hexagonal unit cell with a different, i.e. C_3, symmetry. We first perform topology optimization to obtain a two-fold degeneracy in the bandstructure at the K point. As before, four-node quadrilateral elements are used to discretize the unit cell. The topology is constrained to possess C_3 symmetry, and the volume fraction is again constrained to not fall below 50%. The optimal topology is shown in Fig. 20(a), and the corresponding bandstructure is shown in Fig. 20(b). As seen in Fig. 20(b), a two-fold Dirac degeneracy is obtained at the K point between modes 1 and 2. Furthermore, among the frequency values, the first mode is a maximum and the second mode is a minimum at the K point.

The two-fold degeneracy can be converted to four-fold degeneracy by the zone folding mechanism. The basic unit cell that is obtained is enlarged in order to obtain the four-fold degeneracy at the Γ point. The enlarged unit cell and its band structure are shown in Fig. 21. The enlarged unit cell has to be modified in order to open a band gap and obtain two unit cells with different topological phases. The solid part in the large unit cell (Fig. 21) is rotated by $+30^\circ$ and

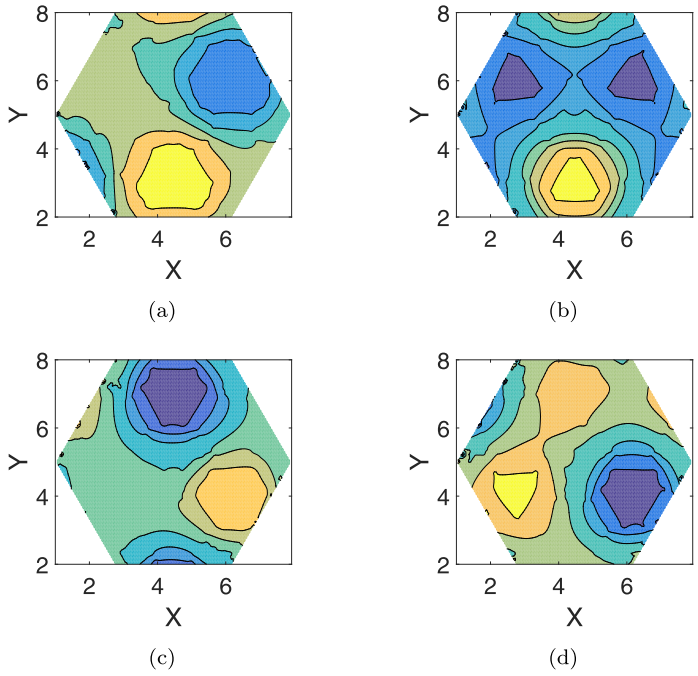

Fig. 25. Eigenmodes of unit cell B, (a) Band 2 (b) Band 3 (c) Band 4 (d) Band 5.

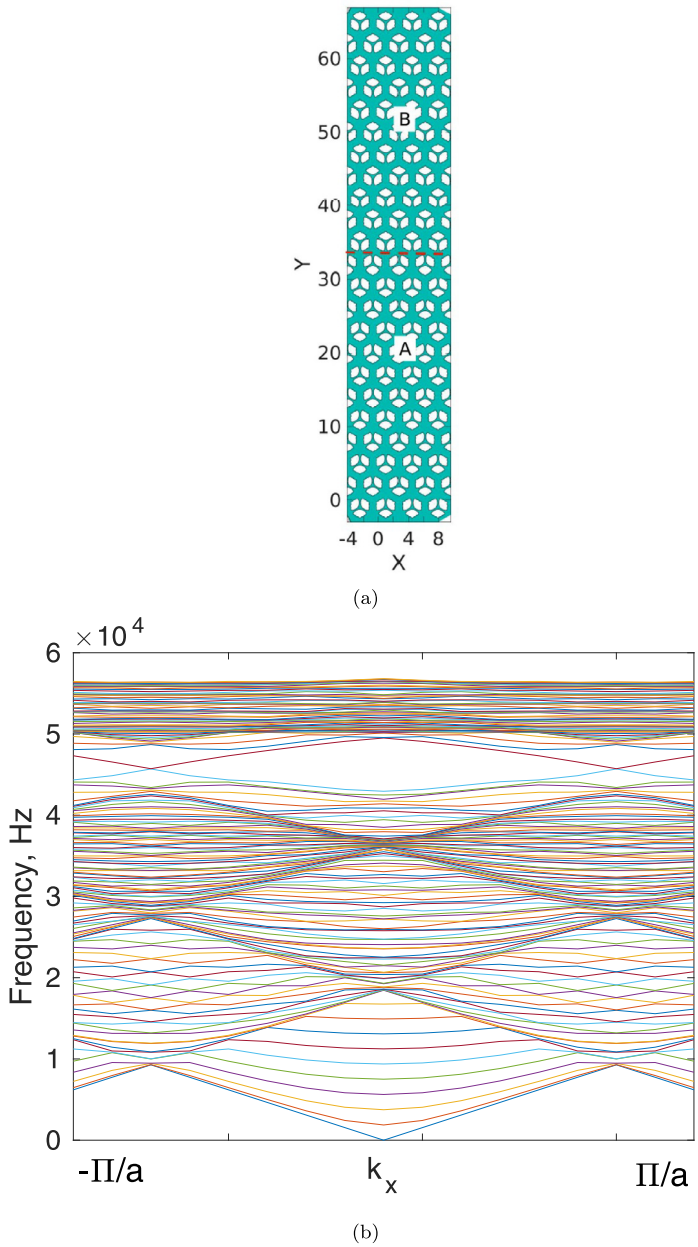

Fig. 26. Supercell comprised of (a) Unit cells A and B and (b) its corresponding band structure. Note the interface mode in the band gap between 44 to 48.5 kHz, and the location of the horizontal interface around Y=32.

$-30°$ in order to obtain two unit cells A and B as shown in Fig. 22. The axis of rotation are the center and corners of the hexagonal unit cell. The band structure of the large unit cells A and B are shown in Fig. 23(a) and 23(b). The band structures of both the unit cells show a gap in the frequency range of 44,000 to 48500 Hz.

The next step is to prove the presence of a band inversion. The eigenmodes of the lower bands of unit cell A shown in Fig. 24(a) and 24(b) are similar to the eigenmodes of the upper bands of unit cells B shown in Fig. 25(c) and 25(d). Similarly, the eigenmodes of the upper bands of unit cell A shown in Fig. 24(c) and 24(d) are similar to the eigenmodes of the lower bands of unit cell B shown in Fig. 25(a) and 25(b).

The supercell shown in Fig. 26(a) is constructed with 12 rows of unit cell A below the interface and 11 rows of unit cell B above the interface. The supercell is periodic in the x-direction and is finite in the y-direction. The band structure corresponding to the supercell is shown in Fig. 26(b). The band structure shows a band gap in the frequency range of 44,000 to 48,500 Hz. Fig. 26(a) also shows interface modes in the band gap, demonstrating the presence of two opposite pseudospin states along the interface in the supercell.

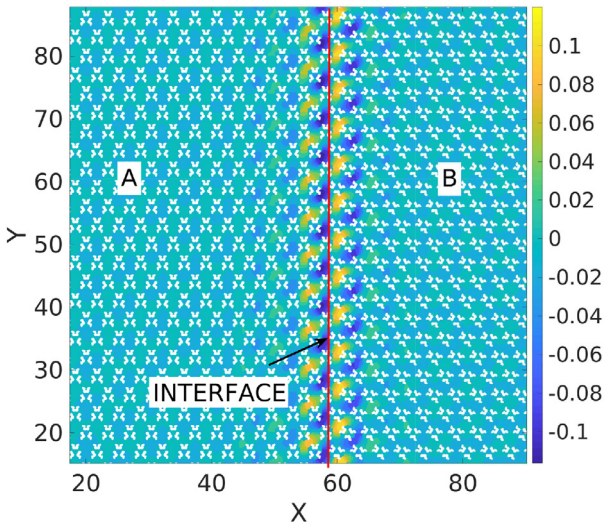

Fig. 27. Displacement contour showing propagation along a straight (vertical) interface. All dimensions are in cm.

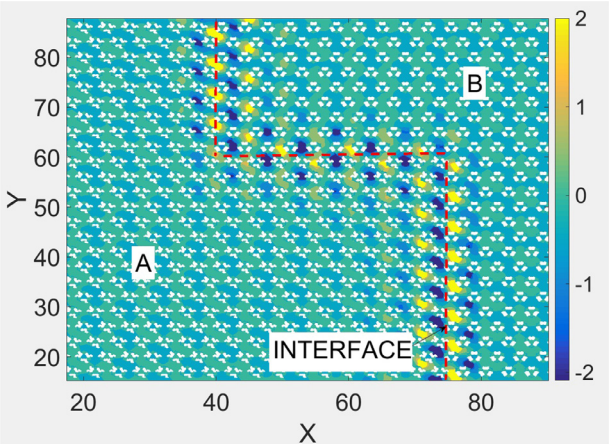

Fig. 28. Displacement contour showing propagation along a zigzag interface. All dimensions are in cm.

The proposed C_3 topology can be tested by solving a wave propagation problem in a periodic structure comprised of unit cells A and B. The resulting periodic structure is made of 17 $\times$ 17 unit cells, and has a straight, vertical interface with 8 columns of A unit cells on one side and 9 columns of B unit cells on the other side. It is excited with a force of amplitude $F_0 = 1$ kN at a frequency of 46,000 HZ. The structure is fixed at y = 0 and excited at y= 104 cm. The displacement field is shown in Fig. 27. It can be clearly seen that the wave penetrates the structure only along the interface while being prevented from entering the bulk. In order to demonstrate the robustness of the designed phononic TI, a complex zig-zag interface is created as shown in Fig. 28, where A unit cells comprise the region to the left of the interface and where B unit cells comprise the region to the right of the interface, the incoming excitation requency is 47 kHz. As shown in Fig. 28, the wave which enters from the top face remains localized to the interface during the propagation to the bottom boundary.

Before concluding, it is worthwhile to compare the topological bandgaps that we have achieved through the inverse design based on C_6 and C_3 symmetries. For the case of C_6 symmetry, the removal of material that is utilized to open a topologically non-trivial bandgap in crystal A and B reduces the topological bandgap of the interface. Specifically, the individual bandgaps of unit cells A and B are 3 kHz (48.5–51.5 kHz) and 3 kHz (46.5 –49.5 kHz) respectively, while the topological bandgap is from 48–50 kHz, i.e. a gap of 2 kHz. On the other hand, for C_3 symmetry the topological bandgap is opened by rotating the crystals rather than by removing or adding mass, and so the difference between individual and effective band gaps is negligible. The band gap of C_3 symmetry unit cells A and B is 4.5 kHz (44–48.5 kHz), which is the same as the topological bandgap of 4.5 kHz. For these reasons, we observe that C_3 symmetry unit cells may offer a wider topologically non-trivial bandgap as compared to C_6 symmetry unit cells.

8. Conclusion

We have proposed a computational inverse design methodology to obtain topologically protected interface modes in structural solids based on the quantum spin hall effect. There are two major steps involved in the approach. The first is to, through a topology optimization approach, implicitly represent the internal boundaries of the structure by a level set function, and subsequently updating the level set front to obtain a topology that gives two-fold degeneracy in the bandstructure. The zone folding approach is then used to map the two-fold (single Dirac cone) degeneracy at the K point onto a four-fold (double Dirac cone) degeneracy at the Γ point in an enlarged unit cell, which captures the degenerate Dirac dispersion required for the two remaining spin states. By breaking translational symmetry, we were able to create two unit cells that, when combined at an interface, were shown to host topologically non-trivial edge states. Real-space numerical examples demonstrated that the interface modes were indeed bound to the interface, and were able to propagate in the presence of defects such as sharp corners, showing the expected robustness of topologically-protected interface phonons.

This approach represents a first step towards designing solid topologically-protected phononic metamaterials of desired symmetry, and we envision that there are future improvements to be made. For example, we have focused on hexagonal unit cells in the present work, and also in obtaining degeneracy between the first two eigenmodes. We believe these conditions can be relaxed in future work, by exploring other unit cell geometries, and the possibility of creating topological bandgaps between any two desired modes. Finally, we have considered only flexural motion in the present work; future work will also consider the more general case of having both in-plane and out-of-plane modes (Mousavi et al., 2015).

Acknowledgments

HSP acknowledges the support of the Army Research Office, grant W911NF-18-1-0380.

Appendix A. Berry Curvature

The Berry curvature for unit cell A with C_6 symmetry for the four bands is shown in Fig. A.29. It can be seen that the Berry curvature of modes 2,3 and 4,5 are of the opposite sign. The transition in the topological phase occurs due to the band inversion between bands 2,3 and 4,5 at Γ point. The integration of each peak or dip gives an area of π or $-\pi$. Dividing by 2π, the contribution from the Berry curvature of each peak or dip to Chern number is $\frac{1}{2}$ or $-\frac{1}{2}$, and thus the spin Chern number is found to be $C_s = \pm 1$.

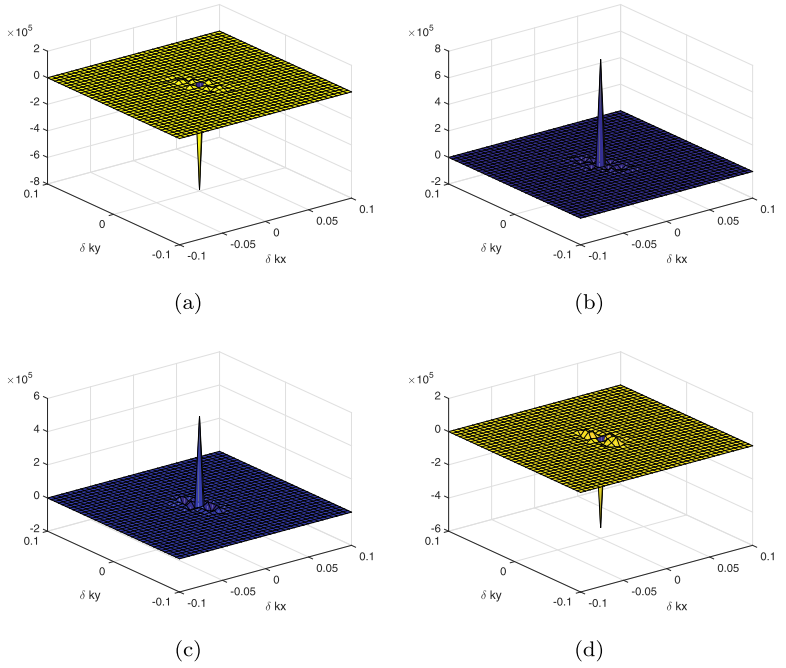

Fig. A.29. Berry Curvature of (a) Band 2 (b) Band 3 (c) Band 4 (d) Band 5.

References

Allaire, G., Jouve, F., Toader, A.-M., 2004. Structural optimization using sensitivity analysis and a level-set method. J. Comput. Phys. 194 (1), 363–393.
Bernevig, B.A., Hughes, T.L., Zhang, S.-C., 2006. Quantum spin hall effect and topological phase transition in HgTe quantum wells. Science 314, 1757–1761.
Berry, M.V., 1984. Quantal phase factors accompanying adiabatic changes. Proceedings of the Royal Society of London A 392, 45–57.
Brendel, C., Peano, V., Painter, O., Marquardt, F., 2018. Snowflake phononic topological insulator at the nanoscale. Phys. Rev. B 97 (2), 020102.
Chen, H., Nassar, H., Huang, G.L., 2018a. A study of topological effects in 1D and 2D mechanical lattices. J. Mech. Phys. Solids 117, 22–36.
Chen, J., Huang, H., Huo, S., Tan, Z., Xie, X., Cheng, J., Huang, G.L., 2018b. Self-ordering induces multiple topological transitions for in-plane bulk waves in solid phononic crystals. Phys. Rev. B 98, 014302.
Chen, Z.-G., Wu, Y., 2016. Tunable topological phononic crystals. Phys. Rev. Appl. 5, 054021.
Cummer, S.A., Christensen, J., Alu, A., 2016. Controlling sound with acoustic metamaterials. Nature Rev. Mater. 1, 1–13.
Deng, Y., Jing, Y., 2017. Zone folding induced topological insulators in phononic crystals. In: Proceedings of the IEEE International Ultrasonics Symposium (IUS). IEEE, pp. 1–4.
Dong, J.-W., Chen, X.-D., Zhu, H., Wang, Y., Zhang, X., 2017. Valley phononic crystals for control of spin and topology. Nature Mater 16, 298–302.
Haldane, F.D.M., 1988. Model for a quantum hall effect without landau levels: condensed-matter realization of the “parity anomaly”. Phys. Rev. Lett 61 (18), 2015–2018.
Hazan, M.Z., Kane, C.L., 2010. Colloquium: topological insulators. Rev Mod Phys 82, 3045–3067.
He, C., Ni, X., Ge, H., Sun, X.-C., Chen, Y.-B., Lu, M.-H., Liu, X.-P., Chen, Y.-F., 2016. Acoustic topological insulator and robust one-way sound transport. Nature Phys. 12, 1124–1129.
Huber, S.D., 2016. Topological mechanics. Nature Phys. 12, 621–623.
Hussein, M.I., Leamy, M.J., Ruzzenne, M., 2014. Dynamics of phononic materials and structures: historical origins, recent progress, and future outlook. Appl. Mech. Rev. 66, 040802.
Jiang, J.-W., Wang, B.-S., Park, H.S., 2018. Topologically protected interface phonons in two-dimensional nanomaterials: hexagonal boron nitride and silicon carbide. Nanoscale 10, 13913–13923.
Kane, C.L., Lubensky, T.C., 2014. Topological boundary modes in isostatic lattices. Nature Phys. 10, 39–45.
Kane, C.L., Mele, E.J., 2005. Quantum spin hall effect in graphene. Phys. Rev. Lett. 95, 226801.
Kariyado, T., Hatsugai, Y., 2015. Manipulation of dirac cones in mechanical graphene. Sci Rep 5, 18107.
Khanikaev, A.B., Fleury, R., Mousavi, S.H., Alu, A., 2015. Topologically robust sound propagation in an angular-momentum-biased graphene-like resonator lattice. Nature Commun. 6, 8260.
Klitzing, K.V., Dorda, G., Pepper, M., 1980. New method for high-accuracy determination of the fine-structure constant based on quantized hall resistance. Phys. Rev. Lett. 45 (6), 494–497.
Konig, M., Wiedmann, S., Brune, C., Roth, A., Buhmann, H., Molenkamp, L.W., Qi, X.-L., Zhang, S.-C., 2015. Quantum spin hall insulator state in HgTe quantum wells. Sci. Rep. 5, 18107.
Li, J., Wang, J., Wu, S., Mei, J., 2017. Pseudospins and topological edge states in elastic shear waves. AIP Adv. 7 (12), 125030.
Li, S., Zhao, D., Niu, H., Zhu, X., Zang, J., 2018. Observation of elastic topological states in soft materials. Nature Commun. 9, 1370.
Liu, T.-W., Semperlotti, F., 2018. Tunable acoustic valley-hall edge states in reconfigurable phononic elastic waveguides. Phys. Rev. Appl. 9, 014001.
Lu, J., Qiu, C., Xu, S., Ye, Y., Ke, M., Liu, Z., 2014. Dirac cones in two-dimensional artificial crystals for classical waves. Phys. Rev. B 89, 134302.
Lubensky, T.C., Kane, C.L., Mao, X., Souslov, A., Sun, K., 2015. Phonons and elasticity in critically coordinated lattices. Rep. Prog. Phys. 78, 073901.
Manchon, A., Koo, H.C., Nitta, J., Frolov, S.M., Duine, R.A., 2015. New perspectives for rashba spin-orbit coupling. Nature Mater 14, 871–882.
van Miert, G., Smith, C.M., 2016. Dirac cones beyond the honeycomb lattice: A symmetry-based approach. Phys. Rev. B 93 (3), 035401. APS
Moore, J.E., 2010. The birth of topological insulators. Nature 464, 194–198.
Mousavi, S.H., Khanikaev, A.B., Wang, Z., 2015. Topologically protected elastic waves in phononic metamaterials. Nature Commun 6, 8682.
Murakami, S., Nagaosa, N., Zhang, S.-C., 2004. Spin-hall insulator. Phys. Rev. Lett. 93 (15), 156804.
Nash, L.M., Kleckner, D., Read, A., Vitelli, V., Turner, A.M., Irvine, W.T.M., 2015. Topological mechanics of gyroscopic metamaterials. Proc. Natl. Acad. Sci. 112 (47), 14495–14500. National Acad Sciences
Nassar, H., Xu, X.C., Norris, A.N., Huang, G.L., 2017. Modulated phononic crystals: non-reciprocal wave propagation and Willis crystals. J. Mech. Phys. Solids 101, 10–29.
Neto, A.H.C., Guinea, F., Peres, N.M.R., Novoselov, K.S., Geim, A.K., 2009. The electronic properties of graphene. Rev. Mod. Phys. 81, 109–162.
Pal, R.K., Ruzzene, M., 2017. Edge waves in plates with resonators: an elastic analogue of the quantum valley hall effect. New J. Phys. 19, 025001.
Pal, R.K., Schaeffer, M., Ruzzene, M., 2016. Helical edge states and topological phase transitions in phononic systems using bi-layered lattices. J. Appl. Phys. 119, 084305.
Pal, R.K., Vila, J., Leamy, M., Ruzzene, M., 2018. Amplitude-dependent topological edge states in nonlinear phononic lattices. Phys. Rev. E 97 (3), 032209. APS
Paulose, J., ge Chen, B.G., Vitelli, V., 2015. Topological modes bound to dislocations in mechanical metamaterials. Nature Phys 11, 153–156.
Prodan, E., Dobiszewski, K., Kanwal, A., Palmieri, J., Prodan, C., 2017. Dynamical majorana edge modes in a broad class of topological mechanical systems. Nature Commun. 8, 14587.
Prodan, E., Prodan, C., 2009. Topological phonon modes and their role in dynamic instability of microtubules. Phys. Rev. Lett. 103, 248101.
Qi, X.-L., Zhang, S.-C., 2010. The quantum spin hall effect and topological insulators. Phys. Today 63, 33–38.
Ren, Y., Qiao, Z., Niu, Q., 2016. Topological phases in two-dimensional materials: a review. Rep. Prog. Phys. 79, 066501.
Rocklin, D.Z., Chen, B.G.-g, Falk, M., Vitelli, V., Lubensky, T.C., 2016. Mechanical weyl modes in topological maxwell lattices. Phys. Rev. Lett. 116, 135503.
Rocklin, D.Z., Zhou, S., Sun, K., Mao, X., 2017. Transformable topological mechanical metamaterials. Nature Commun. 8, 14201.
Süsstrunk, R., Huber, S.D., 2015. Observation of phononic helical edge states in a mechanical topological insulator. Science 349, 47–50.
Süsstrunk, R., Huber, S.D., 2016. Classification of topological phonons in linear mechanical metamaterials. Proc. Natl. Acad. Sci. 113 (33), E4767–E4775. National Acad Sciences
Swinteck, N., Matsuo, S., Runge, K., Vasseur, J.O., Lucas, P., Deymier, P.A., 2015. Bulk elastic waves with unidirectional backscattering-immune topological states in a time-dependent superlattice. J. Appl. Phys. 118, 063103.
Thouless, D.J., Kohmoto, M., Nightingale, M.P., den Nijs, M., 1982. Quantized hall conductance in a two-dimensional periodic potential. Phys. Rev. Lett. 49 (6), 405–408.
Vila, J., Pal, R.K., Ruzzene, M., 2017. Observation of topological valley modes in an elastic hexagonal lattice. Phys. Rev. B 96, 134307.
Wang, J., Zhang, S.-C., 2017. Topological states of condensed matter. Nature Mater 16, 1062–1067.
Wang, P., Lu, L., Bertoldi, K., 2015. Topological phononic crystals with one-way elastic edge waves. Phys. Rev. Lett. 115, 104302.
Wang, S., Wang, M.Y., 2006. Radial basis functions and level set method for structural topology optimization. Int. J. Numer. Methods Eng. 65 (12), 2060–2090.
Wendland, H., 1995. Piecewise polynomial, positive definite and compactly supported radial functions of minimal degree. Adv. Comput. Math. 4 (1), 389–396.
Weng, H., Dai, X., Fang, Z., 2014. Exploration and prediction of topological electronic materials based on first-principles calculations. MRS Bull. 39 (10), 849–858.
Wu, Y., Chaunsali, R., Yasuda, H., Yu, K., Yang, J., 2018. Dial-in topological metamaterials based on bistable stewart platform. Sci. Rep. 8, 112.
Xia, B.-Z., Liu, T.-T., Huang, G.-L., Dai, H.-Q., Jiao, J.-R., Zang, X.-G., Yu, D.-J., Zheng, S.-J., Liu, J., 2017a. Topological phononic insulator with robust pseudospin-dependent transport. Phys. Rev. B 96 (9), 094106.

Xia, Bai-Zhan, Liu, Ting-Ting, Huang, Guo-Liang, Dai, Hong-Qing, Jiao, Jun-Rui, Zang, Xian-Guo, Yu, De-Jie, Zheng, Sheng-Jie, Liu, Jian, 2017b. Topological phononic insulator with robust pseudospin-dependent transport. Phys. Rev. B 96 (9), 094106 APS.
Xiao, M., Ma, G., Yang, Z., Sheng, P., Zhang, Z.Q., Chan, C.T., 2015. Geometric phase and band inversion in periodic acoustic systems. Nature Phys. 11, 240–244.
Yang, Z., Gao, F., Shi, X., Lin, X., Gao, Z., Chong, Y., Zhang, B., 2015. Topological acoustics. Phys. Rev. Lett. 114, 114301.
Yi, G., Youn, B.D., 2016. A comprehensive survey on topology optimization of phononic crystals. Struct. Multidiscip. Optim. 54 (5), 1315–1344.
Yu, S.-Y., He, C., Wang, Z., Liu, F.-K., Sun, X.-C., Li, Z., Lu, H.-Z., Lu, M.-H., Liu, X.-P., Chen, Y.-F., 2018. Elastic pseudospin transport for integratable topological phononic circuits. Nature Commun. 9, 3072.
Zhang, Z., Wei, Q., Cheng, Y., Zhang, T., Wu, D., Liu, X., 2017. Topological creation of acoustic pseudospin multipoles in a flow-free symmetry-broken metamaterial lattice. Physical Review Letters 118, 084303.
Zhu, H., Liu, T.-W., Semperlotti, F., 2018. Design and experimental observation of valley-hall edge states in diatomic-graphene-like elastic wave guides. Phys. Rev. B 97, 174301.